Full length article

Short-range order and its impacts on the BCC MoNbTaW multi-principal element alloy by the machine-learning potential

Pedro A. Santos-Florez [a], Shi-Cheng Dai [b,c], Yi Yao [d,e], Howard Yanxon [a], Lin Li [d,e,*], Yun-Jiang Wang [b,c,*], Qiang Zhu [a,*], Xiao-Xiang Yu [f,g,*]

[a] Department of Physics and Astronomy, University of Nevada, Las Vegas, NV 89154, USA
[b] State Key Laboratory of Nonlinear Mechanics, Institute of Mechanics, Chinese Academy of Sciences, Beijing 100190, China
[c] School of Engineering Science, University of Chinese Academy of Sciences, Beijing 100049, China
[d] Department of Metallurgical and Materials Engineering, University of Alabama, Tuscaloosa, AL 35401, USA
[e] School for Engineering of Matter, Transport and Energy, Arizona State University, Tempe, AZ 85287, USA
[f] Department of Materials Science and Engineering, Northwestern University, Evanston, IL 60208, USA
[g] Novelis Global Research and Technology Center, Kennesaw, GA 30144, USA

ARTICLE INFO

ABSTRACT

We utilize a machine-learning force field, trained by a neural network (NN) with bispectrum coefficients as descriptors, to investigate the chemical short-range order (SRO) influences on the BCC MoNbTaW alloy strengthening mechanism. The NN interatomic potential offers a transferable force field that exhibits accuracy comparable to density functional theory. This innovative NN potential is employed to examine the SRO effects on various aspects such as elasticity, vibrational modes, plasticity, and strength in the MoNbTaW multi-principal element alloy (MPEA). The findings reveal a significant attraction between Mo-Ta pairs, resulting in the formation of locally ordered B2 clusters. These clusters can be adjusted via temperature and enhanced by Nb content. The presence of SRO leads to an increase in high-frequency phonon modes and introduces additional lattice friction to dislocation motion. This approach facilitates efficient compositional screening, paving the way for computational-guided materials design of novel MPEAs with enhanced performance. Furthermore, it opens up avenues for tuning the mechanical properties through optimization of the processing parameters.

1. Introduction

The demand for higher fuel efficiency and lower carbon emission has led to a pressing need to discover, develop, and deploy novel materials that can sustain high mechanical and corrosion damage in extreme environments. After many years of improvements, developing conventional high-temperature materials such as nickel or cobalt-based superalloys, stainless steel, and refractory alloys has plateaued. The emerging multi-principal element alloys (MPEAs) have a vast yet underexplored compositional space, and the numerous combinations of constituents offer considerable freedom in the material design [1–4].

Among a wide range of material properties observed on various compositions and microstructures, some MPEAs have shown exceptional mechanical properties and degradation resistance at elevated temperatures [5–9]. For example, Senkov et al. [10] compared the temperature dependence of the yield stress of NbMoTaW and VNbMoTaW refractory

MPEAs and Ni-based superalloys. The results show the strength of Inconel 718 rapidly decreases above 800 °C. In contrast, the yield stress of the two MPEAs gradually decreases from 600 °C to 1600 °C. Moreover, multiple components combined have a stronger resistance to high-temperature softening than the individual refractory element constituent [11].

Currently, the origin of the distinct properties in the BCC MPEAs remains elusive. Among all the MPEAs' characteristics, chemical short-range order (SRO) has been suggested to play a vital role [12]. Compared to conventional alloys [13–16], MPEAs are likely to exhibit more substantial SRO effects due to the multi-principal components and high concentrations of constituent elements. As such, the local ordering can introduce unusual dislocation slip modes and deformation mechanisms [17], such as the comparable edge and screw dislocations velocities in BCC MPEAs [18], to modify the macroscopic mechanical properties. To verify this hypothesis, it is necessary to conduct a detailed

---

study to characterize the impacts of SRO on the mechanical properties at the atomic level.

Experimental determination of the SRO is exceptionally challenging. Although SRO has been characterized via various scattering technologies (e.g., x-ray, neutron, and electron), more direct observations by advanced electron microscopy became available only recently [19–21]. Regarding the theoretical predictions, people use the cluster expansion approach to expand the alloy's structure into multiple atomic clusters and, through the density functional theory (DFT), calculate energy to determine the interaction coefficient. After that, energy can be calculated for various atomic configurations by Monte Carlo (MC) sampling [22]. Hybrid DFT and MC method was also employed to sample the multi-component solid solutions [23]. DFT-based linear response theory and concentration wave analysis were recently applied to directly predict the SRO and assess the competing long-range order [24].

Despite the efforts mentioned above, the DFT-based methods are difficult to perform large-scale simulations and examine the influences of SRO on the deformation mechanisms. Instead, conventional interatomic potentials were used to study the dislocation structures and mobilities [25]. But this method heavily depends on the availability and reliability of potential models. Meanwhile, several analytic models were developed to provide a generalized prediction [26], but the theory becomes complicated considering the energy contribution beyond the pair interactions.

Recently, machine learning methods have been widely applied in materials modeling. The machine learning potentials (MLPs) are trained by minimizing the cost function to deliberately attune the model to describe the DFT data. The cost of atomistic simulation is orders of magnitude lower than the quantum mechanical simulation, allowing the system to be scaled up to 1 million atoms [27,28]. To date, several regression techniques, including neural networks (NN) [29], Gaussian process regression [30], and linear regression [31,32], are popular choices for MLP development. Compared to other regression techniques, the NN approach has an unbiased mathematical form that can be adapted to any set of reference points through an iterative fitting process on an extensive training data set. To gain better predictive power, several types of symmetry-invariant structure descriptors have been developed to represent the local atomic environment that goes beyond the traditional representation in Cartesian coordinates [33]. Many applications based on different MLP models have shown that the machine learning approach works remarkably well in various atomistic simulations [34–36]. In particular, several MLP models have been developed to investigate the MPEA systems [35–38]. These encouraging results promise using MLP to resolve the dilemma of compromising accuracy and cost for traditional models based on DFT or classical force fields.

In this work, we apply the MLP-aided atomistic simulation to elucidate the fundamental impacts of SRO on the various properties in a model BCC MoNbTaW MPEA through a comprehensive computational attack on the details, including chemical SRO and its temperature dependence, the compositional effects on SRO, the SRO influences on the elastic constants, phonon density of states, generalized stacking fault energies, Peierls stress, and tensile behaviors of the MoNbTaW alloys. The collective results will enable us to understand what matters and what does not and lay the basis for understanding SRO effects. In the following sections, we will introduce MLP development and other necessary computational approaches employed in this study. The MLP is then applied to different simulations (e.g., hybrid molecular dynamics/ Monte Carlo, vibrational analysis, and mechanical deformation) to construct the models with and without SROs and map the relation between SRO and the target mechanical properties. Based on the simulation results, we will discuss the interplay between SRO, phase stability, dislocation core structures, plasticity, and strength. Our general approaches can be used to investigate other MPEA systems and tune the mechanical properties through structure-composition-processing optimization.

2. Machine-learning potential development

Several software packages have been developed to promote the application of MLPs through different protocols [39–43]. Among them, we have developed the PyXtal_FF package [44] that can train different MLP models via the customized choices of machine learning regressions and descriptors. According to our experience with many other systems [44], we chose the NN regression of Spectral Neighbor Analysis Potential (NN-SNAP). This model has been interfaced with the ML-IAP package in the LAMMPS software [45]. In addition to the available data (5529 configurations from MD simulation and special quasi-random structure modeling) in a recent work [37], we added hundreds of configurations with large elastic strains and different crystallographic directions to improve the model's predictive capability. Finally, we carefully designed the model to deal with two extreme scenarios that might appear under high-temperature MD simulations. The first case is the atomic contact at a short distance due to sizable thermal fluctuation. Such configurations are often far from equilibrium and cannot be interpolated by the training data. Therefore, we added an explicit physical term to express the short-range repulsion through the Ziegler-Biersack-Littmark empirical potential [46]. The second case is that a model with a large size may possess defects where the local atoms have low coordination. Such extreme environments have been largely ignored when people construct the DFT training data set from small-size structure periodic models. To address this issue, we also included a set of dimer and trimer configurations (e.g., Mo-Mo, Mo-Ta-Mo with different atomic distances) in our training data to ensure that the trained model understands such distinct environments.

With the augmented data, we performed DFT calculations using the Perdew-Burke-Ernzerhof functional implemented in the VASP code [47], with a plane-wave cutoff energy of 520 eV. For each structure, we computed the SNAP descriptor for each configuration with a band limit ($2j_{max}$) up to 6, corresponding to 30 bispectrum components. The NN training was executed with two hidden layers with 30 nodes for each layer while energy, force, and stress contributions were trained simultaneously. The importance coefficients of force and stress were set to 10^{-3} and 10^{-4}, respectively. The results of the NN potential training are illustrated in Fig. 1. We include 5564 structures and 137, 076 atomic environments for the training data set. The mean absolute errors (MAE) are 3.76 meV/atom for energy, 0.100 eV/A for force, and 0.537 GPa for stress tensors. In addition, our test data set includes 700 structures and 14, 212 atomic environments, which yield the MAE errors of 9.039 meV/atom for energy, 0.117 eV/A for force, and 0.641 GPa for stress tensors. The MLP accuracy is comparable with other recent works [35–37], thus warranting its application for the studies to be discussed in the following sections.

3. Results

3.1. Chemical SRO and its temperature dependence in MoNbTaW

The local chemical orders in BCC MoNbTaW solid-solution alloy were investigated by the LAMMPS software using NN-SNAP. MC swaps of atoms at the specified temperature were performed with the acceptance probability based on the Metropolis criterion [48]. All atoms in the simulation domain were moved using time integration on the Nose-Hoover style and sampled from the canonical ensembles, resulting in a hybrid MC/MD simulation.

To quantify the chemical ordering around a specific element, we calculated the Warren–Cowley (W-C) parameters of the atomic configurations after hybrid MD/MC sampling at different temperatures using the following equation [49]:
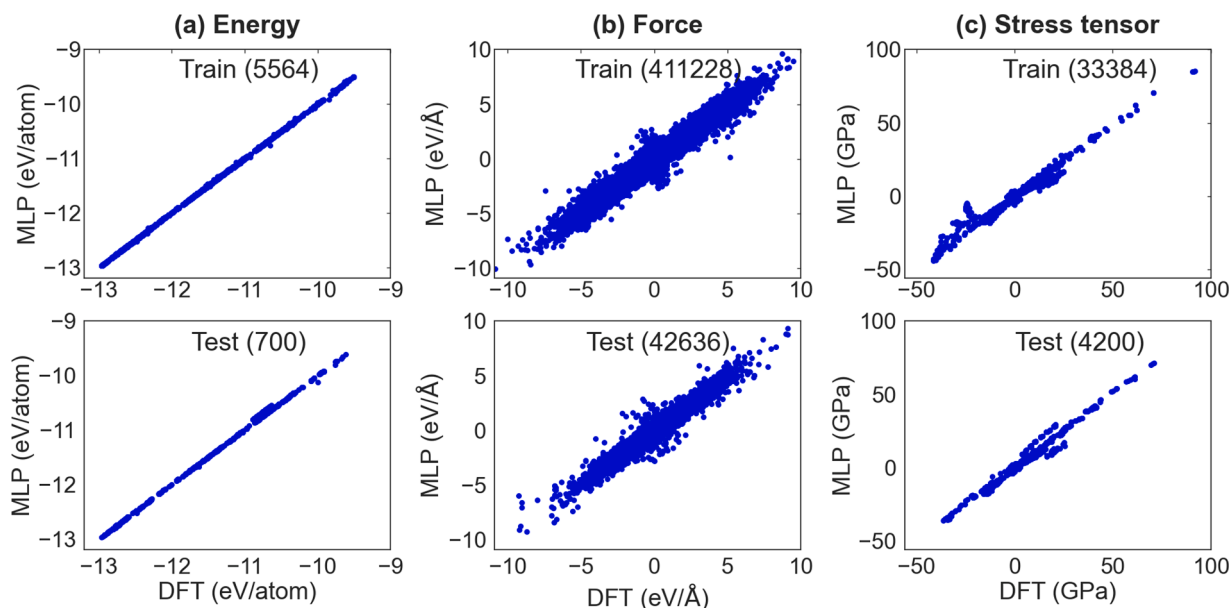
$$\alpha_{ij}^k = 1 - p_{ij}^k \big/ c_j \tag{1}$$

Fig. 1. The performance of (a) energy, (b) force, and (c) stress tensor with training and testing dataset by the current MLP.

where p_{ij}^k is the probability of finding atom i in the kth coordination shell surrounding the atom j. c_j is the nominal concentration of element j. In the case of $\alpha_{ij}^k < 0$, it suggests attractive interactions between the two atom types, while an $\alpha_{ij}^k > 0$ suggests repulsion.

From the results in Fig. 2(a) for various first nearest-neighbors, Mo-Ta, Ta-W, Mo-Nb, and Nb-W pairs show attraction, among others, while Mo-Mo, Ta-Ta, Nb-Ta, and Mo-W pairs show repulsion. Moreover, the SRO is temperature dependent with a disorder-order transition temperature at approximately 1000 K. Above 1000 K, the alloy tends to a random solid solution, and the SRO becomes more potent at lower temperatures below 1000 K. Fig. 2(b) compares the equilibrium atomic configurations at 300 and 1200 K respectively, the squares label the local atomic clusters with B2 structure formed by Mo-Ta pairs. The fraction of short-range B2 order increases as the temperature decreases, which is consistent with our W-C parameters predicted and prior results reported [22,36,37].

In the subsequent investigation of SRO effects, we chose the atomic configurations after MD/MC at 300 and 1200 K as representative

ordered (with SRO) and disordered (without SRO) models and calculated several mechanical properties for comparison. These two types of samples will be referred to as SRO and Random, respectively.

3.2. Element effects on SRO in non-equiatomic alloys

To investigate the alloy composition's impact and multiple elements' synergy effects on the SRO, we constructed several non-equiatomic MoTaNbW quaternaries to evaluate the variation in the local chemical environments. More specifically, we focus on the influence of Nb and W on the Mo-Ta pairs and their local B2 clusters. Two more alloy compositions of $Mo_{25}Ta_{25}Nb_{10}W_{40}$ (i.e., Nb10) and $Mo_{25}Ta_{25}Nb_{40}W_{10}$ (i.e., Nb40) were constructed, where Mo and Ta concentrations were fixed at 25 at.%, and the Nb and W concentrations varied. We simulated five samples for each composition and subjected the samples to a longer annealing time (i.e., an order of magnitude increase in MC steps from 20,000 to 200,000), considering that a higher Nb content could take longer to achieve thermodynamic equilibrium.

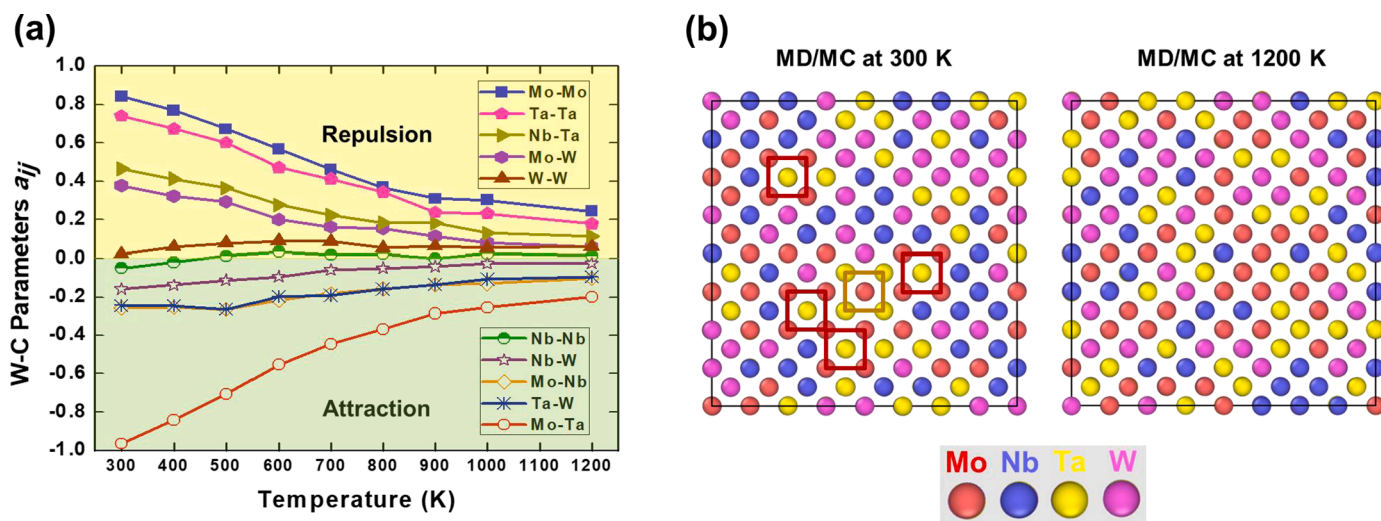Fig. 3a presents the W-C parameters of the Mo-Ta pair in the two

Fig. 2. (a) W-C parameters versus the temperatures in MoNbTaW alloy. (b) Atomic configurations at 300 K and 1200 K after MD/MC sampling, respectively, the red and gold squares label the ordered B2 structures formed by Mo-Ta pairs.
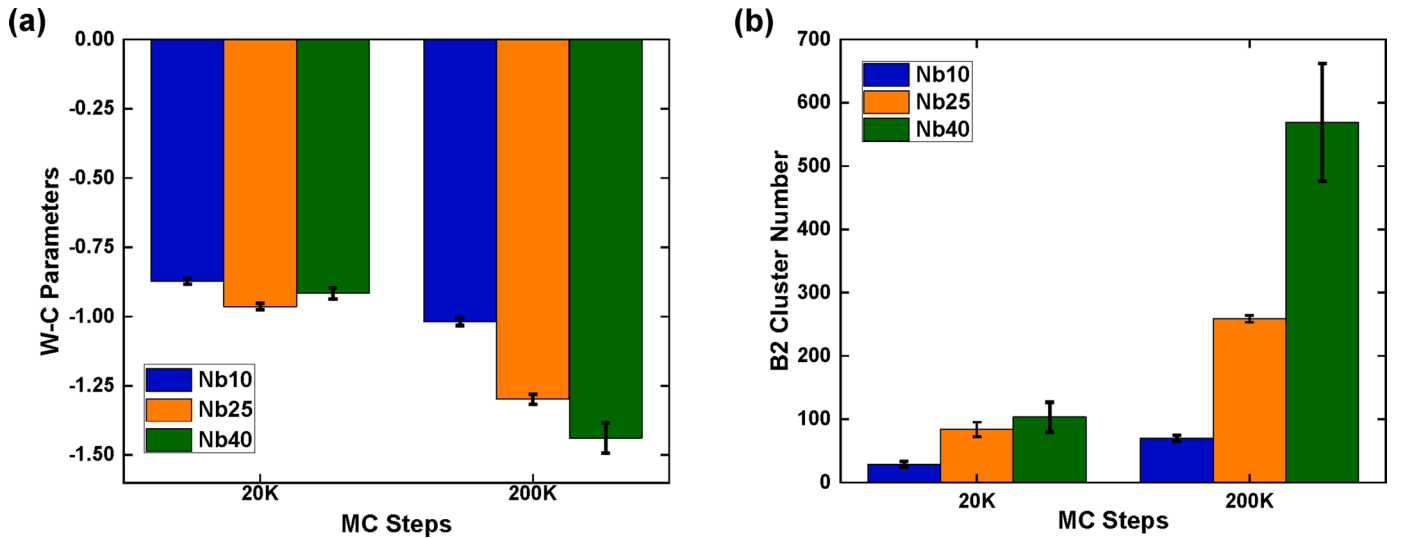
(a)

(b)

Fig. 3. (a) W-C parameters of the Mo-Ta pair, and (b) the number of Mo-Ta local B2 clusters in $Mo_{25}Ta_{25}Nb_{10}W_{40}$ (Nb10), $Mo_{25}Ta_{25}Nb_{25}W_{25}$ (Nb25), and $Mo_{25}Ta_{25}Nb_{40}W_{10}$ (Nb40) alloys subjected to annealing at 300 K for 20, 000 and 200, 000 MC steps.

alloys, along with the equiatomic MoTaNbW for comparison. The W-C parameters of the Mo-Ta pair, especially for longer annealing time, decrease with Nb content in the SRO structures equilibrated at 300 K, indicating Nb enhances the ordering of Mo and Ta. We further counted the number of Mo-Ta B2 clusters in all the alloys, where eight first nearest Mo neighbors surrounded one centered Ta atom and vice versa. As shown in Fig. 3b, the Nb element monotonically increases the Mo-Ta B2 clusters among the three compositions, even though the Mo and Ta concentrations remain unchanged. On the other hand, W exhibits a negative effect on forming the Mo-Ta B2 clusters.

3.3. Elastic constants

In order to understand the elastic behavior under small deformations and the SRO effect, the elastic constants were calculated for samples of BCC MoNbTaW alloys after hybrid MD/MC at 300 and 1200 K. In the first step, the samples containing 8192 atoms were equilibrated with the NPT (isothermal-isobaric) ensemble at zero pressure and a finite temperature varying from 100 to 1200 K for approximately 15 ps. The MD equilibrations were stopped when the fluctuating pressure was closer to zero. In the second step, a negative and a positive strain of 1% was applied separately to the computational cells for each of the Voigt deformation directions (xx→1, yy→2, zz→3, yz→4, xz→5, xy→6). In the final step, the deformed computational cells were equilibrated with the NVT (canonical) ensemble at the same initial temperature for 10 ps. At 0 K, conjugate gradient energy minimizations were performed instead of MD equilibrations.

The resultant average changes in stress were used to compute one row of the elastic stiffness tensor for each Voigt deformation component, considering the average of the negative and positive deformations. Therefore, the elastic constants were calculated using the cubic symmetries as

$$C_{11} = (C_{11} + C_{22} + C_{33})/3 \tag{2}$$

$$C_{12} = (C_{12} + C_{21} + C_{13} + C_{31} + C_{23} + C_{32})/6 \tag{3}$$

$$C_{44} = (C_{44} + C_{55} + C_{66})/3 \tag{4}$$

Fig. 4 shows the elastic constants of the BCC MoNbTaW alloy as a function of temperature obtained from one random and two SRO samples with different initial structures. The results show an approximately linear relationship of the elastic constants with respect to temperature. As expected, the alloys are more compliant at higher temperatures. C_{11}
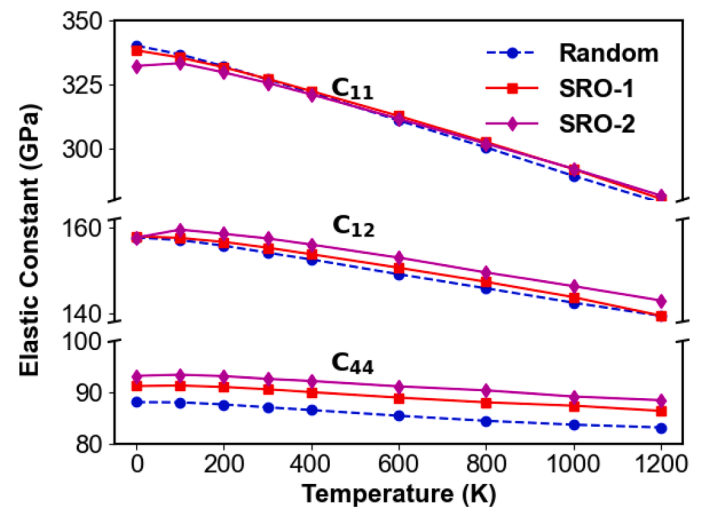

Fig. 4. At various temperatures, the elastic constants of BCC MoNbTaW alloy were obtained from MD/MC simulations for two SRO samples with different initial structures and one random sample.

is more sensitive to temperature, which corresponds to uniaxial deformations. Both SRO samples appear to have consistently higher C_{12} and C_{44} values than the random alloy. For C_{11}, the random solid solution tends to have a bit high value at very low temperatures. Considering the statistical fluctuation, these differences are nearly negligible, indicating that the SRO has a minimal impact on the elastic constants.

3.4. Phonon density of states

To understand the SRO's influence on vibrational properties, we calculated alloy samples' phonon density of states (PDOS) with different degrees of SRO. The PDOS was estimated using the Fourier transform of the velocity-velocity autocorrelation function (VACF) derived from the MD trajectories [50]. This standard procedure is formulated as

$$g(\omega) = \int_0^\infty e^{i\omega t} \frac{\langle \vec{v}(t)\vec{v}(0) \rangle}{\langle \vec{v}(0)\vec{v}(0) \rangle} dt, \tag{5}$$

where ω is the vibrational angular frequency of a normal mode and $g(\omega)$

is the PDOS. $\vec{v}(t)$ is the velocity of an atom at time t, and $\vec{v}(0)$ is the initial velocity. Therefore, the VACF $\langle \vec{v}(t)\vec{v}(0) \rangle$ can be obtained directly from the instant velocity of each atom from the output of any molecular dynamics code. $\langle \cdots \rangle$ denotes an ensemble average. The integral goes sufficiently long to guarantee all the vibrational modes are included. The time resolution should be high enough in simulation to avoid statistical error and huge fluctuation in DOS. Furthermore, the supercell should be large enough to include the long wavelength vibrational mode with low frequency. Our simulation model had 520,000 atoms with $64 \times 64 \times 64$ BCC lattices, which is believed to be large enough to produce physically sound VACF and reliable phonon features [51].

Fig. 5(a) shows the velocity-velocity autocorrelation functions (VACFs) of specific alloys at 10 K. The VACFs decay very quickly and fluctuate around zero within a few picoseconds. The PDOS can be obtained from this feature by Fourier transform according to Eq. (5) and illustrated in Fig. 5(b). Several characteristics can be noticed from the vibrational properties. First, the MD/MLP calculations are reliable if one compares the DOS of a random sample (blue curve) to the reported DFT results (gray area) using a special quasi-random structure supercell model [52]. At very high frequencies above 30 meV, DOS estimated from MLP vanishes, but there are still some high-frequency modes from the DFT prediction. Second, no alloy has the imaginary vibrational frequency, indicating thermodynamically and elastically stable.

Compared to the random structure, the SRO's (red curve) low-frequency modes (mainly corresponding to the elastic waves) remain nearly unchanged; however, the high-frequency modes beyond 25 meV change significantly. The results indicate that SRO enhances the local modulus, and the local hardening may raise extra resistance to the dislocation motion, as shown in the following Peierls stress results. In contrast, the overall modulus, mainly related to low-frequency modes [53,54], will not change much. This is consistent with our aforementioned results that SRO does not remarkably increase elastic constants. We also calculated the Mo-Ta B2 phase (green curve) to compare the long-range order with the SRO effect. The single Mo-Ta B2 phase is apparently of higher frequency, and therefore it is harder than the SRO and random solid solution models.

3.5. Generalized stacking fault energies

Generalized stacking fault (GSF) energies are essential parameters that influence dislocation mobility, deformation twinning, and phase transformation. Here, the GSF energies of the primary slip system $\langle 111 \rangle \{110\}$ in BCC MoNbTaW were performed using a large supercell containing about 36,000 atoms with and without SRO. The supercell was set to be periodic along $\langle 111 \rangle$ and $\langle 112 \rangle$ directions and non-periodic along $\langle 110 \rangle$.

To take into account the local chemical variations, GSF energies were calculated on five consecutive $\{110\}$ planes along with the slip direction $\langle 111 \rangle$, as shown in Fig. 6(a). The averaged GSF in Fig. 6(b) shows that the unstable stacking fault energy (maxima on the GSF energy curve) increases by $\sim$100 mJ/m^2 in the SRO model compared to the random one. The error bars in the energy curves for each displacement indicate the impacts of chemical fluctuation at various locations in this multiple components alloy; however, the variation is less than 20 mJ/m^2. Therefore, the significant contribution to the GSF energy increment and resulting resistance to dislocation slip and dissociation is due to the break of SRO bonding. As an example shown in Fig. 6(a), the Mo-Ta B2 clusters were broken on the (110) slip plane during the shift of two crystal halves relative to each other.

3.6. Peierls stress

To estimate the role of SRO plays in strength, we computed the Peierls stress of a screw dislocation in both ordered and disordered samples. Peierls stress is the threshold stress when dislocation starts to glide at 0 K in an infinite crystal without other defects. It indicates the lattice friction of dislocation, thus a baseline for the strength of metals. For computing the Peierls stress, an athermal quasistatic shear deformation was applied with a small increment of strain 10^{-4} until a critical point where the dislocation started to move. The model was fully relaxed to its local energy minimum at each strain.

For Peierls stress simulation, a $\frac{1}{2}\langle 111 \rangle$ screw dislocation was modeled in the supercell of Fig. 7(a), and the burger vector was along the x [111] direction. The strain-stress curves are shown in Fig. 7(b). Notice that there are a series of stress fluctuations around strain 0.02 in the random structure (blue line). This fluctuation is due to the local structural relaxation rather than Peierls stress. The calculated Peierls stresses in MoNbTaW are 2.47 and 2.91 GPa, for the random and SRO structures, respectively. Therefore the SRO increases the lattice friction of dislocation motion and thus the strength of alloy, which is consistent with the enhancement in high-frequency vibrational modes and GSFs due to SRO.
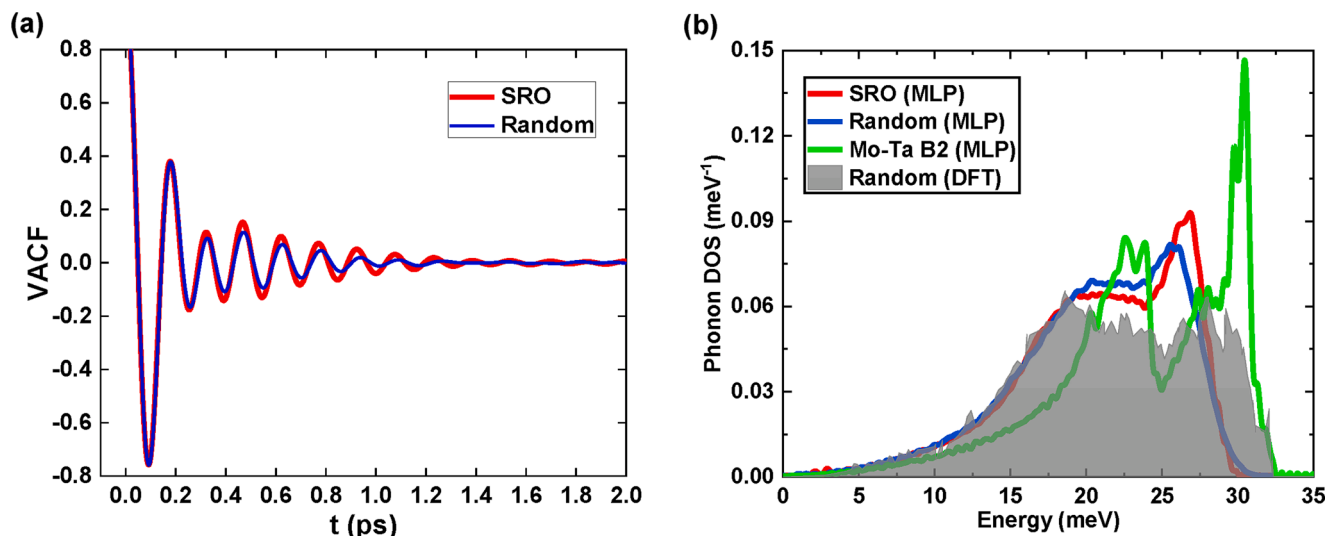

Fig. 5. Vibrational features of BCC MoNbTaW alloy. (a) The VACFs were obtained from MD simulations for samples with the SRO and random ones. (b) Phonon DOS of alloys with different SROs. Normal modes move to high frequency with increasing chemical SRO. MD calculation with the present MLP is validated by DFT calculations on random structures [52].
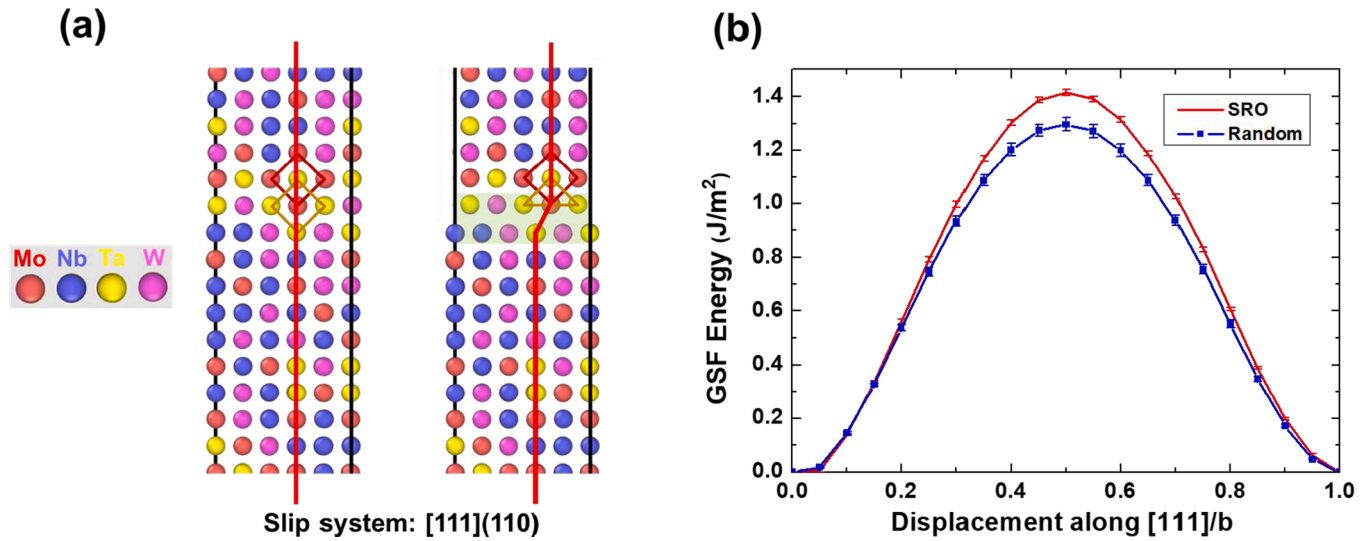
Fig. 6. (a) The side view images of atomic configurations in the original SRO structure and stacking fault. The red and gold squares label the ordered Mo-Ta B2 structures. (b) Averaged GSF of MoNbTaW with and without SRO. The error bars denote chemical fluctuation at various locations.
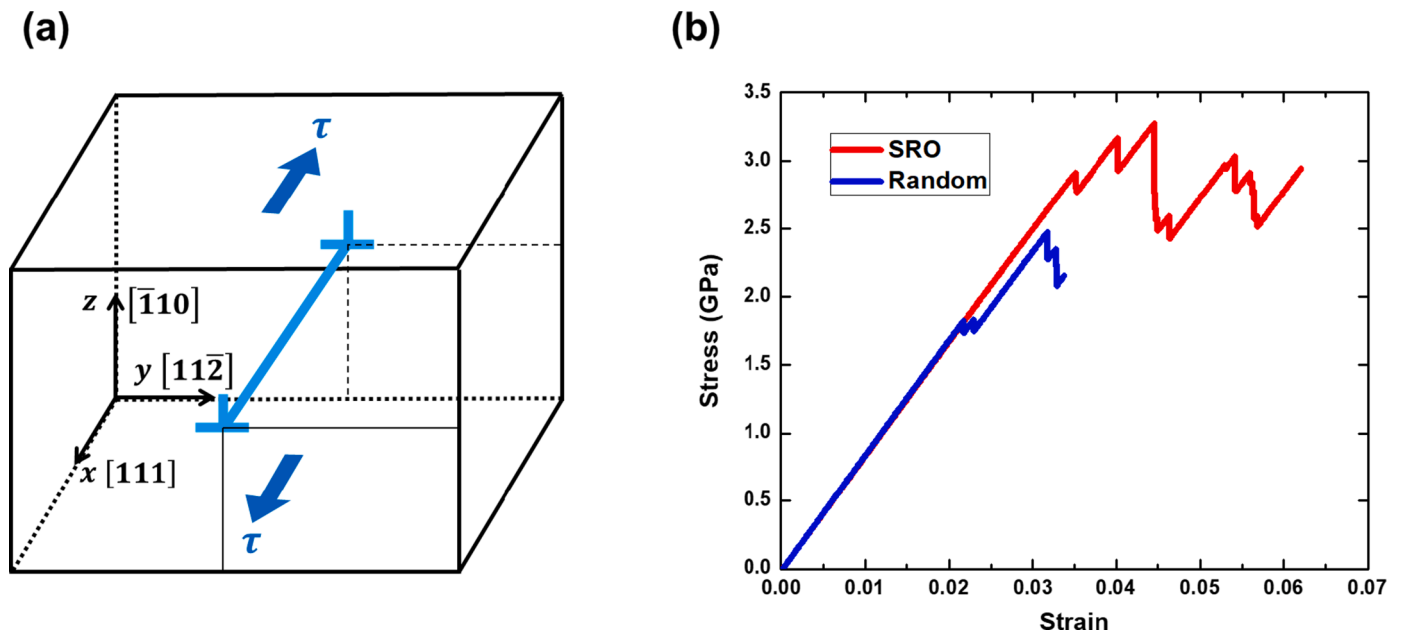

Fig. 7. Resistance of dislocation mobility in MoNbTaW alloys. (a) Schematic illustration of the simulation cell geometry for assessment of Peierls stress of a screw dislocation. (b) Shear stress-strain curves for the SRO and random sample.

3.7. Tensile behaviors

Uniaxial deformations were performed for the tensile strain-stress relations. Before deformation, the samples were equilibrated at zero pressure and the desired temperature with the NPT ensemble for 10 ps. After that, uniaxial tensile deformations were loaded along the [001], [110], and [111] crystallographic directions with a strain rate of 1×10^8 s^{-1}. The stress was measured along the deformation direction, maintaining zero pressure in the transverse directions at a constant temperature. For deformations along the [001] direction, the simulations were carried out using a periodic conventional orthogonal cell containing 8192 atoms with $16 \times 16 \times 16$ BCC lattices. On the other hand, for the deformations along the [110] and [111] directions, a rotated computational cell containing 7128 atoms was used, changing the conventional orthogonal orientations by ([1,1,1], [1,1,−2], [−1,1,0]).

Fig. 8 shows the stress-strain response is anisotropic, depending on

crystallographic orientations. The SRO slightly increases the modulus (slope) in the elastic deformation stage for all three directions, consistent with our previous results. SRO and random samples exhibit similar yield stress. Still, the SRO sample shows more deformation resistance in the [100] and [110], as evidenced by the higher stress level to keep deforming after yielding.

The dominant mechanisms in [110] and [111] directions comply with the dislocation-mediated deformation, as shown in Fig. 8(b) and (c). The majority dislocation type is ½<111> with minor ⟨100⟩ type. The following work hardening after yielding is due to the interplay among the dislocations. In contrast, Fig. 9 presents the [100] tensile stress-strain curve, along with several critical moments denoted on it. No defect was found in the initial sample before the start of the tensile process. It is noted that mechanical instability occurs around a strain of 11% and stress of 16 GPa, driving the simulated sample away from the elastic limit. As the stress increases, <112>{111} twinning is observed
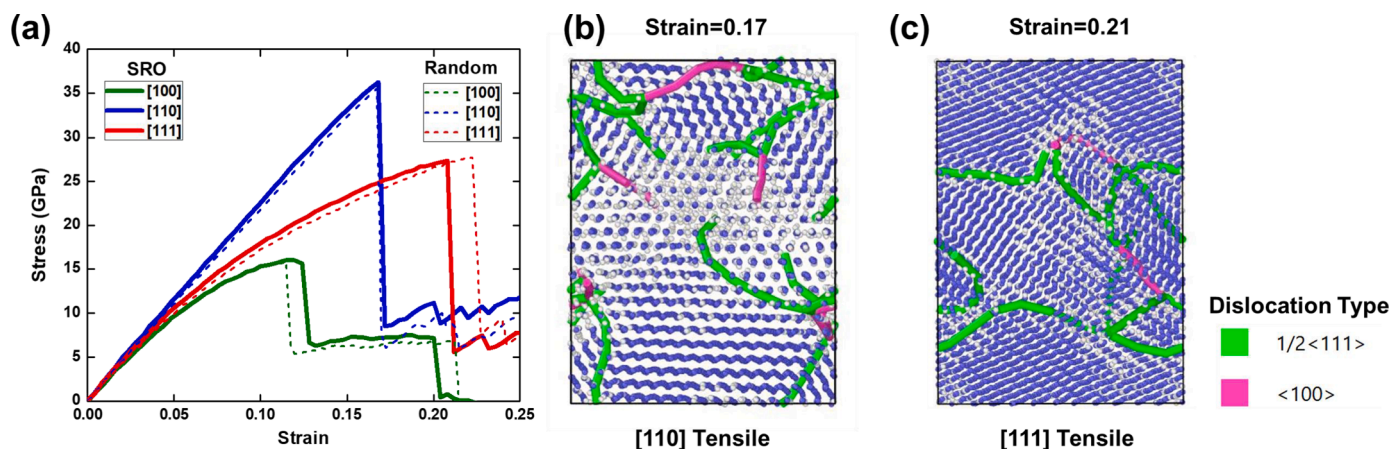
Fig. 8. (a) Uniaxial tensile stress-strain response of the SRO (solid line) and random MoNbTaW (dashed line) samples along [100], [110], and [111] directions at 300 K. Atomic configurations of (b) [110] and (c) [111] tensile strains after yield.
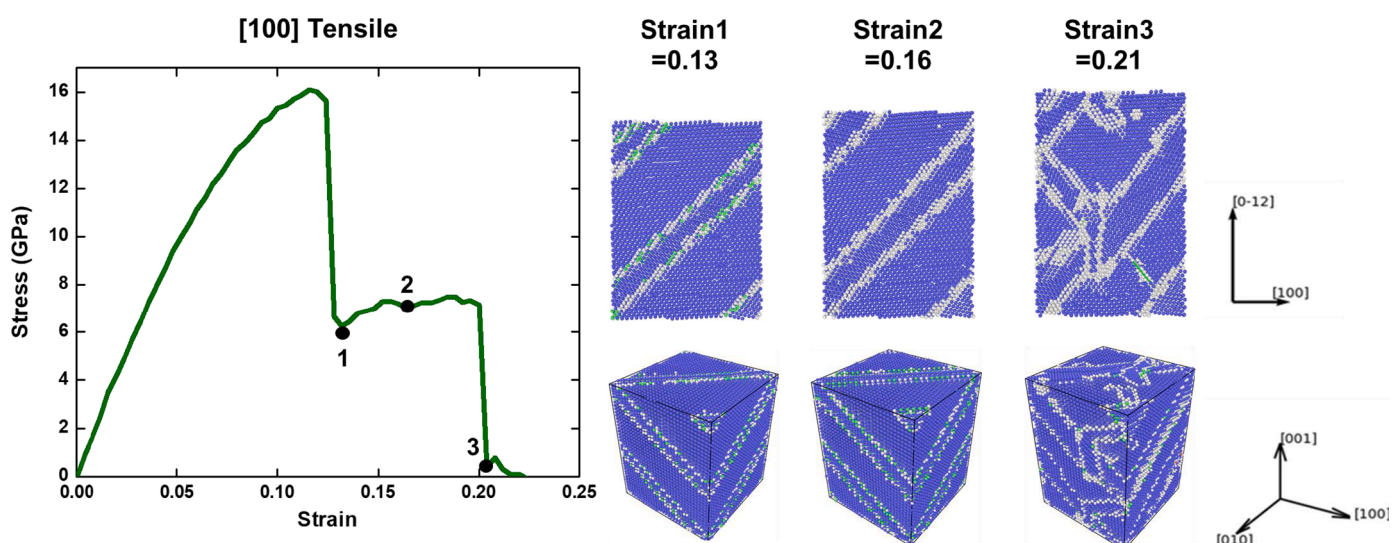

Fig. 9. Atomic configurations at various tensile strains along the [100] direction.

in the crystalline lattice (Fig. 9 Strain=0.13). The first significant stress drop to a lower value of $\sim$ 6.2 GPa, followed by a serration flow with slight hardening. Such stress serration is associated with twin boundary migration (Fig. 9 Strain=0.16). At a strain of 0.2, the second major stress drop occurs, forming a set of cross-twins (Fig. 9 Strain=0.21). Very few dislocation activities are captured. One is shown in Fig. 9 (Strain=0.21), where a dislocation nucleated from one twin boundary, propagated across, and was absorbed by another twin boundary.

4. Discussion

Compared to pure BCC metals and dilute alloys, the strength of some refractory MPEAs exhibits weak temperature dependence over a wide temperature range [10]. Currently, the origin of the outstanding properties doesn't have a clear mechanistic picture. One possible reason is that the multiple principal elements and local chemical fluctuation lead to a rugged energy landscape and considerable variation in barriers of dislocation motion. Another mechanism is through the prevailed SRO in MPEAs, which impacts the structure and mobility of dislocations and enhances the mechanical property. However, the dominant factor in the BCC MPEAs strengthening has yet to be elucidated.

This study scrutinizes the temperature and composition dependence of SRO and their effects on the elastic constants and phonon density of states, generalized stacking fault energies, Peierls stress, and tensile deformation in the MoNbTaW alloys to deconvolute the complexity of strengthening in MPEAs into individual mechanisms. The results show the strong attraction among Mo-Ta pairs forming the short-range ordered B2 clusters. While SRO slightly changes the elastic constants, it evidently redistributes high-frequency phonon modes, which is critical to the material's thermodynamic properties at elevated temperatures.

The remarkable improvement of GSF and Peierls stress indicates SRO's extra lattice friction of dislocation motion besides the multiple principle elements introduced in the rough energy landscape. SRO does not change the twinning initiation in our current [100] tensile deformation compared to the random structure. But it could be expected that the SRO would influence the dislocation structure and velocity after the twin formation.

The strength of BCC MPEAs results from synergistic interactions of various deformation mechanisms influenced by the atomic environment (e.g., SRO), microstructure (e.g., crystallographic orientations), as well as external conditions (e.g., temperature). Here, we reveal a pronounced enhancement in intrinsic lattice resistance of screw dislocation motion due to the presence of SRO despite its minimal effect on elastic constants. However, it is noted that the screw dislocation strengthening processes involve kink-pair nucleation, kink migration, and cross-kink [55]; at high temperatures, thermal diffusion and edge dislocation

motion are hypothesized to gain importance in BCC MPEAs [56]. Whether SRO will strengthen the alloy depends on specific compositions and their interaction with the dislocation [57]. Moreover, crystallographic orientations are vital in deformation mechanisms, microstructure evolution, and dislocation activities. Deformation-induced twinning is favored in tensile loading along [100] directions, whereas dislocation activities dominate along [110] and [111] directions. Therefore, our results suggest a tailorable grain texture along with tunable chemical orders collectively impact the mechanical behaviors of BCC MPEAs.

Rich in SROs is one of the salient features inherent to MPEAs, distinguishing them from traditional alloys. Experimentally, the MPEAs are processed, homogenized, and annealed at temperatures below their melting points, unavoidably accommodating SROs [4]. Tuning the SROs could offer a new strategy to tailor novel multi-component alloys' structural, chemical, magnetic, and mechanical properties. In CrCoNi FCC alloys, it has been shown that tempering to promote SRO has increased hardness, enhanced SFE, and a subsequent increase in planar slip [20]. Similarly, our temperature dependence results map out the tunable SRO degree in MoNbTaW with temper, which facilitates processing optimization to achieve the alloy's applicable property.

In addition to thermal processing, we demonstrate that properly designing the alloy composition by increasing Nb content can enhance the chemical SRO and local Mo-Ta B2 clusters in the non-equiatomic MoTaNbW alloys. Considering that Nb is the lightest element in the MoTaNbW system and further promotes the SRO effect, it is reasonable to anticipate an enhanced specific strength, which guides the experimentalists in the composition search of this refractory alloy for lightweight applications.

All the aforementioned simulations heavily rely on the availability of the MLP model. Our MLP model is similar to the previous efforts based on linear regression [35,36]. However, we believe that using neural networks makes the model more flexible in capturing target functions' nonlinear behavior, such as the potential energy surface. More importantly, the execution cost of NN is similar to linear regression when the same set of descriptors is used. Therefore, it is perhaps more suitable for large-scale simulation of multiple-component systems in which nonlinear effects are more pronounced.

Moreover, it is essential to remember that nearly all MLP models suffer from the extrapolation problem. A typical MLP model is usually trained with the atomic configurations near the equilibrium. Therefore, it cannot reasonably extrapolate the non-equilibrium configurations with either too short or too long atomic distances. In our experience, the inclusion of dimer data and explicit repulsion terms can generally prevent the explosion of MD simulation due to MLP's nonphysical prediction when the system departs strongly from the equilibrium. In addition, one should never apply the model to predict the configuration that has not yet been considered in the training process. Although our initial MLP model correctly predicted all elastic and vibrational properties and the deformation responses in the [100] direction, it yielded an unphysical amorphization behavior for the deformation at [110] and [111]. To improve the MLP, we intentionally included more deformation configurations in our training database. This example highlights the extrapolation challenge in MLP development. It is essential to ensure that the simulation stays within the training domain for diverse application cases. This precaution is necessary to maintain the reliability and accuracy of the simulation results across different scenarios and applications. Otherwise, the training database must be fed additional data to guarantee the model's interpolative capability. Only when the training data has been efficiently sampled the MLP-based interpolation can be considered a compelling solution to bridge the gap between DFT and classical force field simulations.

5. Conclusion

In summary, we report the application of well-trained MLP to simulate the model MPEA system of MoNbTaW. We trained a neural network potential based on a large set of structure-properties data and MD configurations from DFT calculation. Combining the MLP with hybrid molecular dynamics/Monte Carlo simulations, we thoroughly investigate the impacts of SRO on phase stability, dislocation core structures, plasticity, and strength in the MoNbTaW MPEA. In addition to the MoNbTaW with equal proportions, the combination of MLP with other contemporary computational techniques is also suitable for rapidly screening target compounds in a vast compositional space, thus paving the way for computation-guided materials design of new MPEAs with better performance.

Declaration of Competing Interest

The authors declare that they have no known competing financial interests or personal relationships that could have appeared to influence the work reported in this paper.

References

[1] J.W. Yeh, S.K. Chen, S.J. Lin, J.Y. Gan, T.S. Chin, T.T. Shun, C.H. Tsau, S.Y. Chang, Nanostructured high-entropy alloys with multiple principal elements: novel alloy design concepts and outcomes, Adv. Eng. Mater. 6 (5) (2004) 299–303.

[2] Y. Zhang, T.T. Zuo, Z. Tang, M.C. Gao, K.A. Dahmen, P.K. Liaw, Z.P. Lu, Microstructures and properties of high-entropy alloys, Prog. Mater. Sci. 61 (2014) 1–93.

[3] D.B. Miracle, O.N. Senkov, A critical review of high entropy alloys and related concepts, Acta Mater. 122 (2017) 448–511.

[4] E.P. George, D. Raabe, R.O. Ritchie, High-entropy alloys, Nat. Rev. Mater. 4 (8) (2019) 515–534.

[5] O. Senkov, G. Wilks, D. Miracle, C. Chuang, P. Liaw, Refractory high-entropy alloys, Intermetallics 18 (9) (2010) 1758–1765.

[6] F. Granberg, K. Nordlund, M.W. Ullah, K. Jin, C. Lu, H. Bei, L. Wang, F. Djurabekova, W. Weber, Y. Zhang, Mechanism of radiation damage reduction in equiatomic multicomponent single phase alloys, Phys. Rev. Lett. 116 (13) (2016), 135504.

[7] B. Gludovatz, A. Hohenwarter, D. Catoor, E.H. Chang, E.P. George, R.O. Ritchie, A fracture-resistant high-entropy alloy for cryogenic applications, Science 345 (6201) (2014) 1153–1158.

[8] Z. Li, K.G. Pradeep, Y. Deng, D. Raabe, C.C. Tasan, Metastable high-entropy dual-phase alloys overcome the strength–ductility trade-off, Nature 534 (7606) (2016) 227–230.

[9] X.X. Yu, M.A. Taylor, J.H. Perepezko, L.D. Marks, Competition between thermodynamics, kinetics and growth mode in the early-stage oxidation of an equimolar CoCrFeNi alloy, Acta Mater. 196 (2020) 651–659.

[10] O.N. Senkov, G.B. Wilks, J.M. Scott, D.B. Miracle, Mechanical properties of Nb25Mo25Ta25W25 and V20Nb20Mo20Ta20W20 refractory high entropy alloys, Intermetallics 19 (5) (2011) 698–706.

[11] F. Wang, G.H. Balbus, S. Xu, Y. Su, J. Shin, P.F. Rottmann, K.E. Knipling, J. C. Stinville, L.H. Mills, O.N. Senkov, Multiplicity of dislocation pathways in a refractory multiprincipal element alloy, Science 370 (6512) (2020) 95–101.

[12] E. Ma, Unusual dislocation behavior in high-entropy alloys, Scr. Mater. 181 (2020) 127–133.

[13] J. Spruiell, E. Stansbury, X-ray study of short-range order in nickel alloys containing 10.7 and 20.0 at.% molybdenum, J. Phys. Chem. Solids 26 (5) (1965) 811–822.

[14] N. Clement, D. Caillard, J. Martin, Heterogeneous deformation of concentrated Ni-Cr FCC alloys: macroscopic and microscopic behaviour, Acta Metall. 32 (6) (1984) 961–975.

[15] K. Buschow, Short-range order and thermal stability in amorphous alloys, J. Phys. F Met. Phys. 14 (3) (1984) 593.

[16] V. Gerold, H. Karnthaler, On the origin of planar slip in fcc alloys, Acta Metall. 37 (8) (1989) 2177–2183.

[17] F. Otto, A. Dlouhý, C. Somsen, H. Bei, G. Eggeler, E.P. George, The influences of temperature and microstructure on the tensile properties of a CoCrFeMnNi high-entropy alloy, Acta Mater. 61 (15) (2013) 5743–5755.

[18] B. Chen, S. Li, H. Zong, X. Ding, J. Sun, E. Ma, Unusual activated processes controlling dislocation motion in body-centered-cubic high-entropy alloys, Proc. Natl. Acad. Sci. 117 (28) (2020) 16199–16206.

[19] Q. Ding, Y. Zhang, X. Chen, X. Fu, D. Chen, S. Chen, L. Gu, F. Wei, H. Bei, Y. Gao, Tuning element distribution, structure and properties by composition in high-entropy alloys, Nature 574 (7777) (2019) 223–227.

[20] R. Zhang, S. Zhao, J. Ding, Y. Chong, T. Jia, C. Ophus, M. Asta, R.O. Ritchie, A. M. Minor, Short-range order and its impact on the CrCoNi medium-entropy alloy, Nature 581 (7808) (2020) 283–287.

[21] X. Chen, Q. Wang, Z. Cheng, M. Zhu, H. Zhou, P. Jiang, L. Zhou, Q. Xue, F. Yuan, J. Zhu, X. Wu, E. Ma, Direct observation of chemical short-range order in a medium-entropy alloy, Nature 592 (7856) (2021) 712–716.

[22] A. Fernández-Caballero, J. Wróbel, P. Mummery, D. Nguyen-Manh, Short-range order in high entropy alloys: theoretical formulation and application to Mo-Nb-Ta-VW system, J. Ph. Equilibria Diffus. 38 (4) (2017) 391–403.

[23] J. Ding, Q. Yu, M. Asta, R.O. Ritchie, Tunable stacking fault energies by tailoring local chemical order in CrCoNi medium-entropy alloys, Proc. Natl. Acad. Sci. 115 (36) (2018) 8919–8924.

[24] P. Singh, A.V. Smirnov, A. Alam, D.D. Johnson, First-principles prediction of incipient order in arbitrary high-entropy alloys: exemplified in Ti0. 25CrFeNiAlx, Acta Mater. 189 (2020) 248–254.

[25] S. Rao, B. Akdim, E. Antillon, C. Woodward, T. Parthasarathy, O. Senkov, Modeling solution hardening in BCC refractory complex concentrated alloys: nbTiZr, Nb1. 5TiZr0. 5 and Nb0. 5TiZr1. 5, Acta Mater. 168 (2019) 222–236.

[26] Y. Rao, W. Curtin, Analytical models of short-range order in FCC and BCC alloys, Acta Mater. 226 (2022) 117621.

[27] N. Artrith, J. Behler, High-dimensional neural network potentials for metal surfaces: a prototype study for copper, Phys. Rev. B 85 (4) (2012), 045439.

[28] W. Li, Y. Ando, E. Minamitani, S. Watanabe, Study of Li atom diffusion in amorphous Li3PO4 with neural network potential, J. Chem. Phys. 147 (21) (2017), 214106.

[29] J. Behler, Constructing high-dimensional neural network potentials: a tutorial review, Int. J. Quantum Chem. 115 (16) (2015) 1032–1050.

[30] A.P. Bartók, G. Csányi, G aussian approximation potentials: a brief tutorial introduction, Int. J. Quantum Chem. 115 (16) (2015) 1051–1057.

[31] A.V. Shapeev, Moment tensor potentials: a class of systematically improvable interatomic potentials, Multiscale Model. Simul. 14 (3) (2016) 1153–1173.

[32] A.P. Thompson, L.P. Swiler, C.R. Trott, S.M. Foiles, G.J. Tucker, Spectral neighbor analysis method for automated generation of quantum-accurate interatomic potentials, J. Comput. Phys. 285 (2015) 316–330.

[33] A.P. Bartók, R. Kondor, G. Csányi, On representing chemical environments, Phys. Rev. B 87 (18) (2013), 184115.

[34] Y. Zuo, C. Chen, X. Li, Z. Deng, Y. Chen, J.R. Behler, G. Csányi, A.V. Shapeev, A. P. Thompson, M.A. Wood, Performance and cost assessment of machine learning interatomic potentials, J. Phys. Chem. A 124 (4) (2020) 731–745.

[35] S. Yin, Y. Zuo, A. Abu-Odeh, H. Zheng, X.G. Li, J. Ding, S.P. Ong, M. Asta, R. O. Ritchie, Atomistic simulations of dislocation mobility in refractory high-entropy alloys and the effect of chemical short-range order, Nat. Commun. 12 (1) (2021) 1–14.

[36] T. Kostiuchenko, F. Körmann, J. Neugebauer, A. Shapeev, Impact of lattice relaxations on phase transitions in a high-entropy alloy studied by machine-learning potentials, npj, Comput. Mater. 5 (1) (2019) 1–7.

[37] X.G. Li, C. Chen, H. Zheng, Y. Zuo, S.P. Ong, Complex strengthening mechanisms in the NbMoTaW multi-principal element alloy, npj Comput. Mater. 6 (1) (2020) 1–10.

[38] X. Wang, F. Maresca, P. Cao, The hierarchical energy landscape of screw dislocation motion in refractory high-entropy alloys, Acta Mater. 234 (2022) 118022.

[39] A. Singraber, T. Morawietz, J.R. Behler, C. Dellago, Parallel multistream training of high-dimensional neural network potentials, J. Chem. Theory Comput. 15 (5) (2019) 3075–3092.

[40] K. Lee, D. Yoo, W. Jeong, S. Han, SIMPLE-NN: an efficient package for training and executing neural-network interatomic potentials, Comput. Phys. Commun. 242 (2019) 95–103.

[41] A. Khorshidi, A.A. Peterson, Amp: a modular approach to machine learning in atomistic simulations, Comput. Phys. Commun. 207 (2016) 310–324.

[42] Y. Shao, M. Hellström, P.D. Mitev, L. Knijff, C. Zhang, PiNN: a python library for building atomic neural networks of molecules and materials, J. Chem. Inf. Model. 60 (3) (2020) 1184–1193.

[43] K.T. Schütt, H.E. Sauceda, P.J. Kindermans, A. Tkatchenko, K.R. Müller, Schnet–a deep learning architecture for molecules and materials, J. Chem. Phys. 148 (24) (2018), 241722.

[44] H. Yanxon, D. Zagaceta, B. Tang, D.S. Matteson, Q. Zhu, PyXtal_FF: a python library for automated force field generation, Mach. Learn. Sci. Technol. 2 (2) (2020), 027001.

[45] S. Plimpton, Fast parallel algorithms for short-range molecular dynamics, J. Comput. Phys. 117 (1) (1995) 1–19.

[46] J.F. Ziegler, J.P. Biersack, The Stopping and Range of Ions in matter, Treatise on Heavy-Ion Science, Springer, 1985, pp. 93–129.

[47] G. Kresse, J. Furthmüller, Efficient iterative schemes for ab initio total-energy calculations using a plane-wave basis set, Phys. Rev. B 54 (16) (1996) 11169.

[48] W.K. Hastings, Monte Carlo sampling methods using Markov chains and their applications, Biometrika 57 (1970) 97–109.

[49] B.E. Warren, X-Ray Diffraction, Courier Corporation, 1990.

[50] J. Dickey, A. Paskin, Computer simulation of the lattice dynamics of solids, Phys. Rev. 188 (3) (1969) 1407.

[51] J. Yang, Y.J. Wang, E. Ma, A. Zaccone, L. Dai, M. Jiang, Structural parameter of orientational order to predict the boson vibrational anomaly in glasses, Phys. Rev. Lett. 122 (1) (2019), 015501.

[52] M.C. Gao, P. Gao, J.A. Hawk, L. Ouyang, D.E. Alman, M. Widom, Computational modeling of high-entropy alloys: structures, thermodynamics and elasticity, J. Mater. Res. 32 (19) (2017) 3627–3641.

[53] P.A. Geslin, D. Rodney, Microelasticity model of random alloys. part I: mean square displacements and stresses, J. Mech. Phys. Solids 153 (2021), 104479.

[54] P.A. Geslin, A. Rida, D. Rodney, Microelasticity model of random alloys. part II: displacement and stress correlations, J. Mech. Phys. Solids 153 (2021), 104480.

[55] F. Maresca, W.A. Curtin, Theory of screw dislocation strengthening in random BCC alloys from dilute to "High-Entropy" alloys, Acta Mater. 182 (2020) 144–162.

[56] F. Maresca, W.A. Curtin, Mechanistic origin of high strength in refractory BCC high entropy alloys up to 1900 K, Acta Mater. 182 (2020) 235–249.

[57] E. Antillon, C. Woodward, S. Rao, B. Akdim, Chemical short range order strengthening in BCC complex concentrated alloys, Acta Mater. 215 (2021), 117012.